

Measurements of the Microstructural, Microchemical and Transition Temperature Gradients of A15 layers in High Performance Nb₃Sn PIT Superconducting Strand

C D Hawes¹, P J Lee and D C Larbalestier

The Applied Superconductivity Center, The University of Wisconsin-Madison, Madison, WI 53706-1609, USA

¹Now at August Technology, Bloomington, MN 55435, USA

E-mail: lee@engr.wisc.edu

Abstract. There has been a remarkable increase in layer critical current density, J_c , for Nb₃Sn in the past 5 years. At ~ 5000 A/mm² (12 T, 4.2 K), the average layer critical current density is now double that of the best ITER-Central Solenoid Model Coil strand. The improvements in critical current density are a result of increased Sn content in the superconducting A15 phase and better compositional homogeneity and perhaps of other reasons not yet understood. The first indication that such large increases in Nb₃Sn layer critical were possible was in powder-in-tube strand produced by Shape Metal Innovations, SMI. The design of these strands allows us to accurately measure the composition gradient as well as the gradient in critical temperature across the A15 layer and we reports these measurements here for a wide range of heat treatments. Inductive T_c measurements were used to measure the radial gradient of T_c , while specific heat measurements revealed the position-insensitive inhomogeneity of the A15 layer. Composition gradients were measured by Energy Dispersive X-Ray Spectroscopy in a Field Emission Scanning Electron Microscope. The three characterizations show that the composition and T_c gradient is quite shallow near the central Sn source and only becomes steep adjacent to the Nb sheath of each filament, a result that is beneficial to maximizing the fraction of the layer with high T_c . This strong non-linearity of the T_c and composition gradient means that excellent properties are obtained, in spite of the in-built composition gradients inevitable in any filamentary design of composite. The gradients are much smaller than reported for bronze-route conductors but higher than the overall layer gradient found in the latest generation of high critical current density internal Sn design strands. Coupled to recent modelling simulations our data show the great value of high Sn designs in developing high layer J_c values in Nb₃Sn conductors.

1. Introduction

Nb₃Sn superconducting composites are now commercially fabricated in long lengths by three approaches: the bronze route [1], the internal-tin route [2], and the powder-in-tube, PIT, approach. In recent years there has been a remarkable increase in the highest critical current density, J_c , values achieved in commercial internal Sn process Nb₃Sn strand with 12 T (4.2 K) non-Cu J_c s close to [3] or exceeding [4] 3000 A/mm². The increased J_c values result from a $\sim 70\%$ increase in the critical current density of the A15 layer, $J_{c(sc)}$ compared with the Nb₃Sn strand used for the ITER CS Model Coil [5,6]. The first indication that substantial increases in $J_{c(sc)}$ were obtainable was in strand produced by SMI in The Netherlands using the

ECN-PIT approach, whose value has been well demonstrated in its use for high field dipoles [7]. The commercially available PIT design starts with NbSn₂, Sn and Cu powder encased in Nb or Nb alloy tubes, which are then stacked into a billet and either drawn or extruded to form a multifilamentary wire. PIT conductors achieved the first 12 T (4.2 K) non-copper J_c values exceeding 2100 A/mm² [8] and have been optimized to as high as 2250 A/mm² [9], more than double that available in bronze conductors or with low-hysteresis-loss design internal tin conductors. PIT strands also have a more uniform geometry than bronze process strands and have a smaller effective filament diameter than high J_c internal Sn strands. The flexibility of the PIT approach is demonstrated by another recent PIT design, which used a mixture of

Nb_6Sn_5 and Nb powder in Ta tubes, which were groove- and flat-rolled into a tape having B_{c2} values of 24.7 T at 4.2 K and J_c values of 330 A/mm² at 20 T and 4.2 K [10]. Here, we exploit the geometrical uniformity and magnetically transparent filament design of the SMI-PIT strand, in order to directly measure the variation in T_c across the A15 layer and correlate that with measurements of the compositional gradient.

As the maximum possible performance is sought in A15 compound wires, designers must deal with the difficulty of simultaneously obtaining optimum stoichiometry of the A15 phase (the phase exists over the range Nb 25-18 at.% Sn, the T_c varying linearly from 18 to 6 K over this range [11]), a sufficiently fine grain structure for strong flux pinning, and a strain state that does not depress the T_c too much throughout as much of the A15 layer as is possible. Since conventional methods (e.g. bronze or internal Sn process) of making Nb_3Sn end with A15 layers that are typically less than 2 μm in thickness, of variable composition and grain morphology [12-16], and with a strong precompression from the bronze around each filament, it is seldom clear how much of each filament is actually carrying current, particularly at high fields. As the primary flux-pinning centres in Nb_3Sn are the grain boundaries, more aggressive heat treatments that offer the potential to increase chemical homogeneity, have the undesired effect of reducing the grain boundary density (and thus flux pinning) due to grain growth.[17] The "inside-out" design of PIT strands makes them magnetically transparent, since the highest T_c shell is on the inside, exposing the T_c gradient to magnetic measurements. Furthermore the precursor, Sn-rich, NbSn_2 phase of the core reacts rapidly to make an A15 layer that is thick enough, $\sim 5 \mu\text{m}$, to permit quantitative analysis of the chemical gradient by Energy Dispersive X-ray Spectroscopy (EDS) in the scanning electron microscope. Another advantage is that the Nb filament shell has a low thermal contraction coefficient, which is well matched to that of the Nb_3Sn , thus minimizing T_c and B_{c2} precompression effects applied by the surrounding Cu matrix.

T_c was measured both by DC magnetization in a manner permitting its positional variation to be determined and by specific heat where this information is absent. These techniques provide complementary information about the variation of T_c . SEM-EDS analysis of Nb and Sn can provide an accuracy of better than ± 1 at.% over lengths as small as $\sim 1 \mu\text{m}$, thus providing a positional sensitivity of order 0.5 K/ μm , given the linear variation of T_c with composition, ~ 1.7 K/at.% Sn [11]. Both

superconducting measurements have temperature sensitivity of better than 0.1 K. The inductive T_c measurements are sensitive to T_c variations on a scale of a few penetration depths, λ (λ is $\sim 0.25 \mu\text{m}$ at 4 K), while the specific heat is determined on the coherence length scale, that is ~ 3 nm at 4 K. Thus both superconducting measurements are capable of observing T_c variations on scales small compared to the filament dimensions and the spatial resolution of SEM-EDX measurements.

2. Experimental Details

2.1. Conductor Details

The PIT conductor was manufactured by ShapeMetal Innovations (SMI), The Netherlands [8], [18]. The conductor contains 504 very uniform Nb-tube filaments, figure 1a, containing a powder mixture of NbSn_2 , Sn and Cu. Image analysis reveals the composite's high quality, as the average cross-sectional area variation among 50 filaments was found to be less than 5 % at the final wire diameter of 0.90 mm (where the Nb filament diameter was $\sim 27 \mu\text{m}$). A rounded hexagonal shape was imparted to the filaments during fabrication. As noted later this leads to certain filament non-uniformities in longer time reactions. The matrix was pure Cu.

Wires were examined at 0.90 mm diameter. For reaction they were sealed in evacuated quartz tubes and heat treated at the SMI-recommended temperature of 675°C [8] for up to 263 hours. Heat treatments at 750°C up to 110 hours were also performed in order to assess the terminal reaction state of the composite.

2.2. Inductive Critical Temperature Measurements

The magnetization of 5-7 mm long sections of reacted wires was measured in a Quantum Design SQUID magnetometer with the applied magnetic field parallel to the wire axis. Samples were weighed so that their magnetization could be determined to an accuracy of better than 1%. This geometry has a negligible demagnetization factor and full flux shielding can be calculated rather closely. Samples were cooled to 5 K in zero field and a 1 mT field then applied, the magnetic moment then being measured every 0.1 K on heating until the transition temperature was exceeded. The moment of the sample is determined by the annulus which is superconducting at any temperature. This annulus also includes the volume of the residual Sn-Cu powder core shielded by the superconductor.

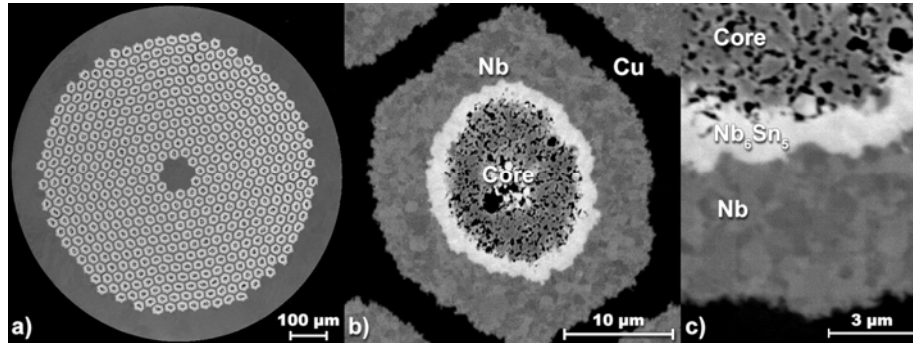


Figure 1. SEM-BES images of SMI 504 filament PIT composite wire, a) overview and b) and c) filament details after 2 hr heat treatment at 675°C showing the Nb₆Sn₅ layer before Nb₃Sn formation.

Assuming that the annulus is fully diamagnetic, its weak field susceptibility is:

$$M / H = -1 / 4\pi \quad (1)$$

where M is the volume magnetization and H is the applied field. Neglecting the hexagonal symmetry of the 504 Nb filaments, we approximate the superconducting annuli as right circular cylinders, permitting us to write the shielded volume as:

$$V = 504\pi r_{sc+core}^2(T) l \quad (2)$$

where l is the sample length and $r_{sc+core}(T)$ is the radial thickness of the superconductor and the shielded non-superconducting core at temperature T . As noted above, this core must be included, since the highest T_c layer lies right next to the core and thus shields the core up to the maximum T_c . Substituting (2) into (1), and expressing M in terms of the measured magnetic moment, $m (=MV)$ gives:

$$r_{sc+core} = 2 \times \sqrt{\frac{m}{504HI}} \quad (3)$$

Strictly speaking, full diamagnetism is only obtained for layers 5-10 penetration depths, λ , thick [19]. The approximation discussed above thus becomes less valid as T tends to T_c , as is discussed later.

2.3. Heat Capacity Measurements

The superconducting phase transition is a second-order transition characterized by a sharp jump in the heat capacity at T_c for a homogeneous material. An inhomogeneous material will yield a smeared transition that can be used to directly measure the distribution of T_c values on a scale of the coherence length, ξ , that is

~ 3 nm at 4 K. The heat capacity of 3-6 mg wire samples was measured using a Quantum Design relaxation calorimeter [20],[21] operating in zero field, cooling from 30 K or 22 K to 5 K. Samples were cut or ground to < 1 cm in length, so as to fit the sample platform. A small smear of Apiezon grease aided the thermal conductance between the sample and the sample platform. The heat capacity of the platform with the Apiezon grease was measured to define the addenda correction, which was subsequently subtracted from the total heat capacity when the sample was present.

Measurement of the whole wire results in the heat capacity of all components of the wire, e.g. Cu, residual Sn and Nb in the core and filaments, and A15, when what are actually desired are the electronic

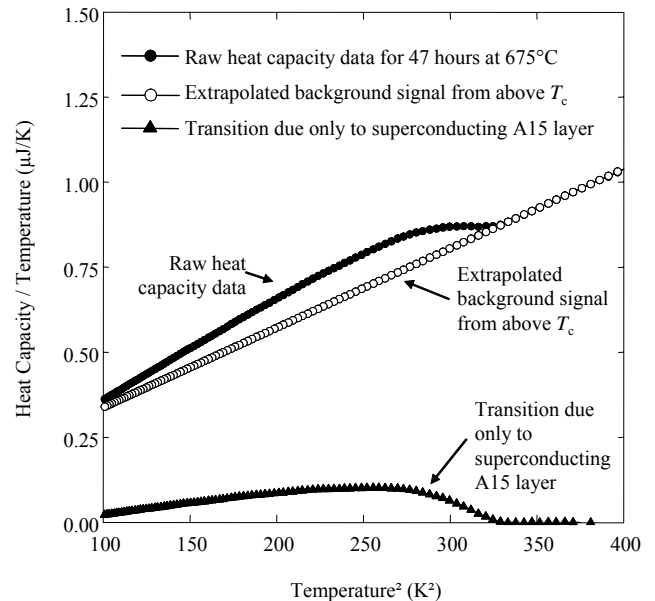


Figure 2. The filled circles are the raw heat capacity data for the SMI PIT conductor heat treated at 675°C for 47 hours. The open circles are the linear extrapolation of the background signal. The filled triangles are the heat capacity data for the A15 layer, which results from the subtraction of the two curves.

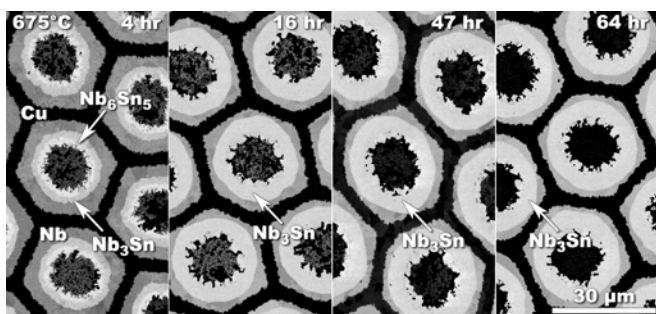


Figure 3. Atomic number sensitive electron backscatter images of the after 4, 16, 47, and 64 hours at 675°C. In the cross-section for the 4 hour heat treatment, the light gray layer near the core is Nb₆Sn₅, the next darker gray layer is Nb₃Sn, the outermost layer is Nb, and the black matrix is Cu. In the 16, 47, and 64 hour images, the gray layer near the core is Nb₃Sn, the next darker layer is Nb, and the black matrix is Cu.

transitions of the superconducting layer. In fact these normal metal components all had good cubic temperature dependence of their specific heat, permitting linear extrapolation of the greater-than- T_c data in a C/T vs. T^2 plot to lower T , as is shown graphically in figure 2.

2.4. SEM-BSE/EDX Measurements

The backscatter electron (BSE) signal in the Scanning Electron Microscope (SEM) is atomic number sensitive, allowing accurate measurement of layer thicknesses in metallographically polished cross-sections. Most of the BSE images were obtained using a JEOL JSM-6100 SEM at 10 kV at a working distance

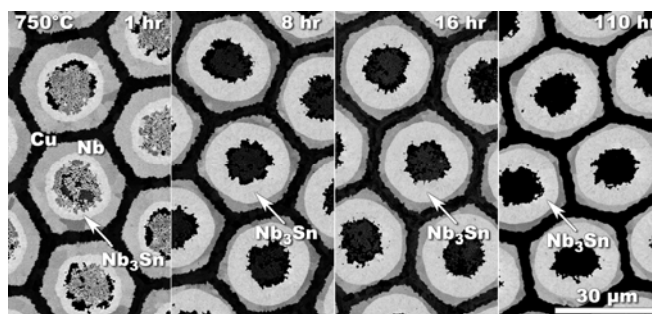


Figure 4. Electron backscatter images after 1, 8, 16, and 110 hours, at 750°C. The black matrix is Cu, the darker gray regions are Nb, and the lighter gray regions are Nb₃Sn.

of 15 mm. Fracture images of the grain structure were obtained using either a LEO-982 field emission scanning electron microscope (FESEM) or a LEO-1530 FESEM at 3 kV and a working distance of 3 mm for the LEO-1530 and 6 mm for the LEO-982. Energy dispersive x-ray (EDX) analysis was performed on either the LEO-982 or the LEO-1530 at 8 kV and a working distance of 9 mm. Compositions were derived from the Nb-L and Sn-L peaks by standardless analysis, performed by the Noran Instruments Voyager analysis system.

3. Results

3.1. SEM-BSE/EDX and Microstructural Measurements

Backscatter electron images and EDX analysis of the

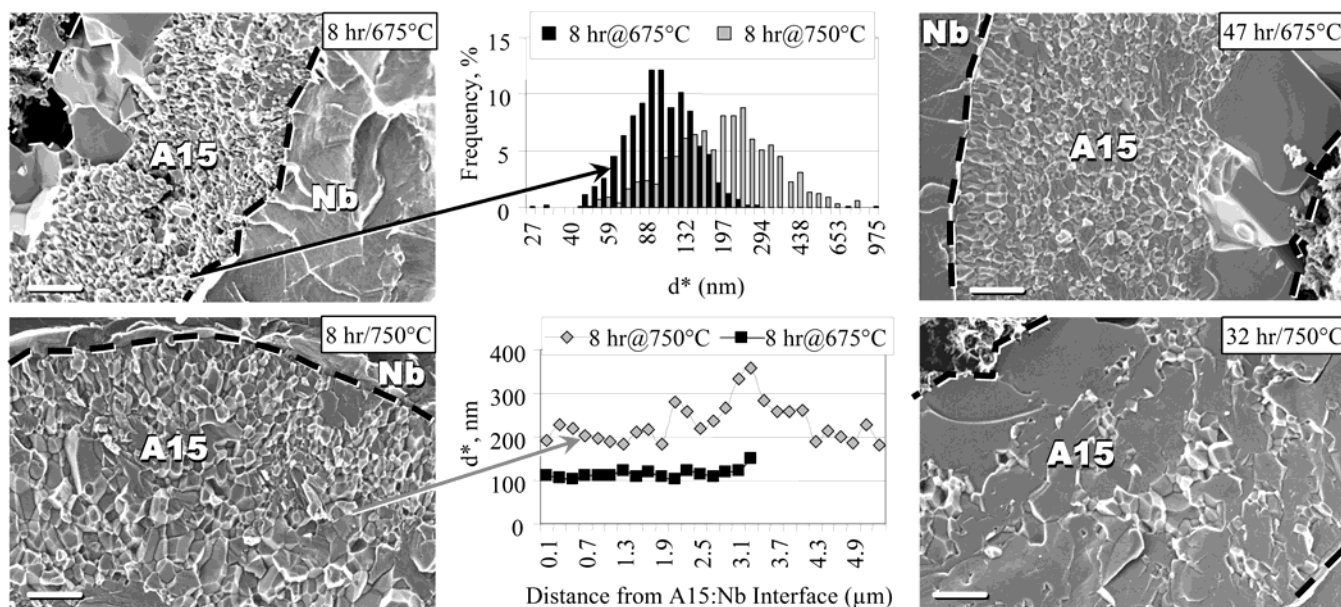


Figure 5. SEM fractographs of partial filament cross-sections for 4 different heat treatments. The scale bars are 1 μ m in length. Insets are quantitative comparisons of the A15 grain size distributions after reactions of 8 hrs at 675°C and 750°C.

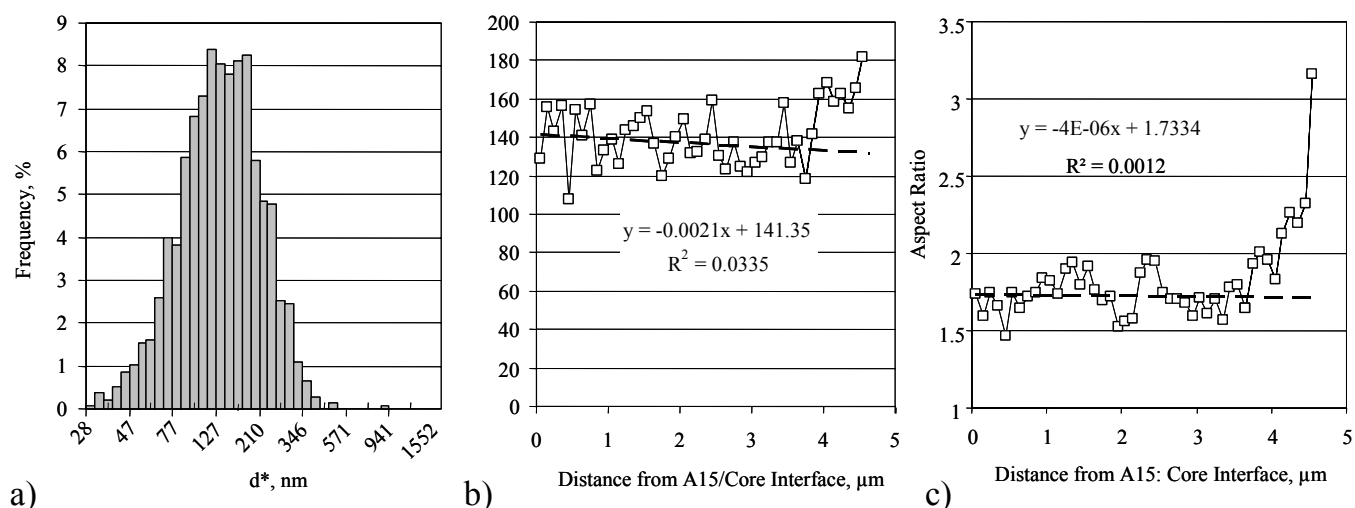


Figure 6. Quantitative microstructural analysis of a fine-grain A15 layer after heat treatment for 47 hr at 675°C. In a) we show that the d^* distribution is ln-normal. The grain size (d^*) and aspect ratio change across the A15 layer are plotted in b) and c) respectively. Least squares fits to the inner 3.5 μm suggest a slight decline in both d^* and aspect ratio across this range. After 3.5 μm there is a sharp increase in aspect ratio.

2 hour heat treatment at 675°C show that a layer of Nb_6Sn_5 forms during the first stages of the reaction between the NbSn_2 -containing powder core and the Nb tube (figures 1b and 1c). The progress of the reaction at 675°C of the powder core and the Nb is shown in figure 3. After 4 hours, both Nb_6Sn_5 and Nb_3Sn regions are visible, but the Nb_6Sn_5 disappears after 16 hours. At 47 hours the A15 layer is only a little thicker than at 16 hours, but A15 phase has clearly reached the Nb-Cu interface at some thinner regions between the hexagonal edges of each filament. 64 hours of reaction produced little additional growth in A15 layer thickness, which then attained about 5 μm . The progress of the reaction at 750°C is shown in figure 4. After 1 hour the A15 layer is visible but reaction was so fast that little Nb_6Sn_5 remains. At 16 hours the layer is only slightly thicker than at 8 hours, and the A15 phase has reached the Nb-Cu interface in places.

The fracture images in figure 5 show that both the 8 and 47 hour at 675°C samples have large, approximately 1-2 μm size, A15 grains near the core. The larger grain layer is typically only a single A15 grain thick. Outside this larger grain layer is a layer of much smaller grains. The grain size distribution (expressed here as d^* , the diameter of the fine A15 grains calculated from their transverse cross-sectional areas assuming a circular cross-section) is log-normal. In the top inset of figure 5 we compare the d^* distribution after 8 hrs for the 675°C and 750°C heat treatment. The mean d^* for the fine grain A15 layer after 8 hr at 675°C is only 120 nm compared to 196 nm for 750°C. In the lower inset chart we plot the grain size (d^*) as a function of distance from the A15:Nb

interface for the same two samples using the positional normalizing technique described in [22]. The grain size is quite uniform across the layer for the 675° sample but there is considerable non-uniformity at 750°C. After 32 hours at 750°C the grain size has grown very considerably, and now approaches a large fraction of the layer thickness.

In figure 6 we illustrate the quantitative microstructural analysis of the fine-grain A15 layer after 47 hr at 675°C. In figure 6a) we show that the d^* distribution is ln-normal with a \ln^{-1} mean d^* of 127 nm. Using the ln-normal data we are able to describe the $\pm\sigma$ range as 79-330 nm. The grain size (d^*) and aspect ratio change across the A15 layer are plotted in figure 6b and 6c respectively. 1382 grains were analyzed from a fractograph analyzed with respect to the distance of their centroids with respect to the core:A15 layer interface. Least squares fits to the inner 3.5 μm suggest a slight decline in both d^* and aspect ratio across this range. Outside the 3.5 μm thick inner annulus there is a sharp increase in aspect ratio. The change to higher aspect ratio implies a lower A15 grain nucleation rate and is typical of low-Sn A15 as seen in bronze process strand.

The results of the EDX analysis are shown in figure 7. Vertical error bars represent the 2σ error based on the measured x-ray peak intensities, while the horizontal error bars represent the positional uncertainty defined by the variation in the Sn-rich core shape and the contamination spot left by the electron-beam-surface interaction. The LEO-1530 exhibited significant positional drift over the course of the measurement, resulting in the larger horizontal error

bars for the 750°C / 110 hour heat treatment.

A Sn-composition gradient was observed in all measurements, the shortest reactions having the steepest gradient. Although the gradients are not strictly linear (especially near the A15-Nb interface which is not sampled here), a straight line was fit to each data set to provide a simple measure of the influence of increasing reaction. The gradients declined markedly as reaction became more complete: -0.92 at.%/μm (8 hr/675°C), -0.69 at.%/μm (16 hr/675°C), -0.64 at.%/μm (47 hr/675°C), and -0.37 at.%/μm (110 hrs/750°C). The onset of the increased aspect ratio observed for 47 hr at 675°C in figure 6c can be correlated with a Sn composition drop of 2.2 at.% Sn using the gradient of -0.64 at.%/μm.

3.2. Inductive Critical Temperature Measurements

The strong initial A15 layer growth rate can also be directly inferred from the inductive critical temperature plots in figures 8a and 8b for the 650°C and 750°C heat treatments respectively. Full flux exclusion from within each filament was seen at 5 K in all samples. The lower transition occurs at ~9 K when the Nb filament sheath goes normal. However, the normalized magnetic moment curves in figure 9 indicate that this “Nb transition temperature” decreases and broadens with increasing heat treatment time. In agreement with the backscatter electron images in figure 4, no significant A15 phase was found after 2 hours at 675°C, but significant growth was found at 4 hours. By contrast, even 1 hour at 750°C produced significant A15 growth. At both 675°C and 750°C, increasing the heat treatment time results in a steady rise in the maximum T_c , a thickening of the layer, and a flattening in the A15 T_c gradient. Some apparent deviations from

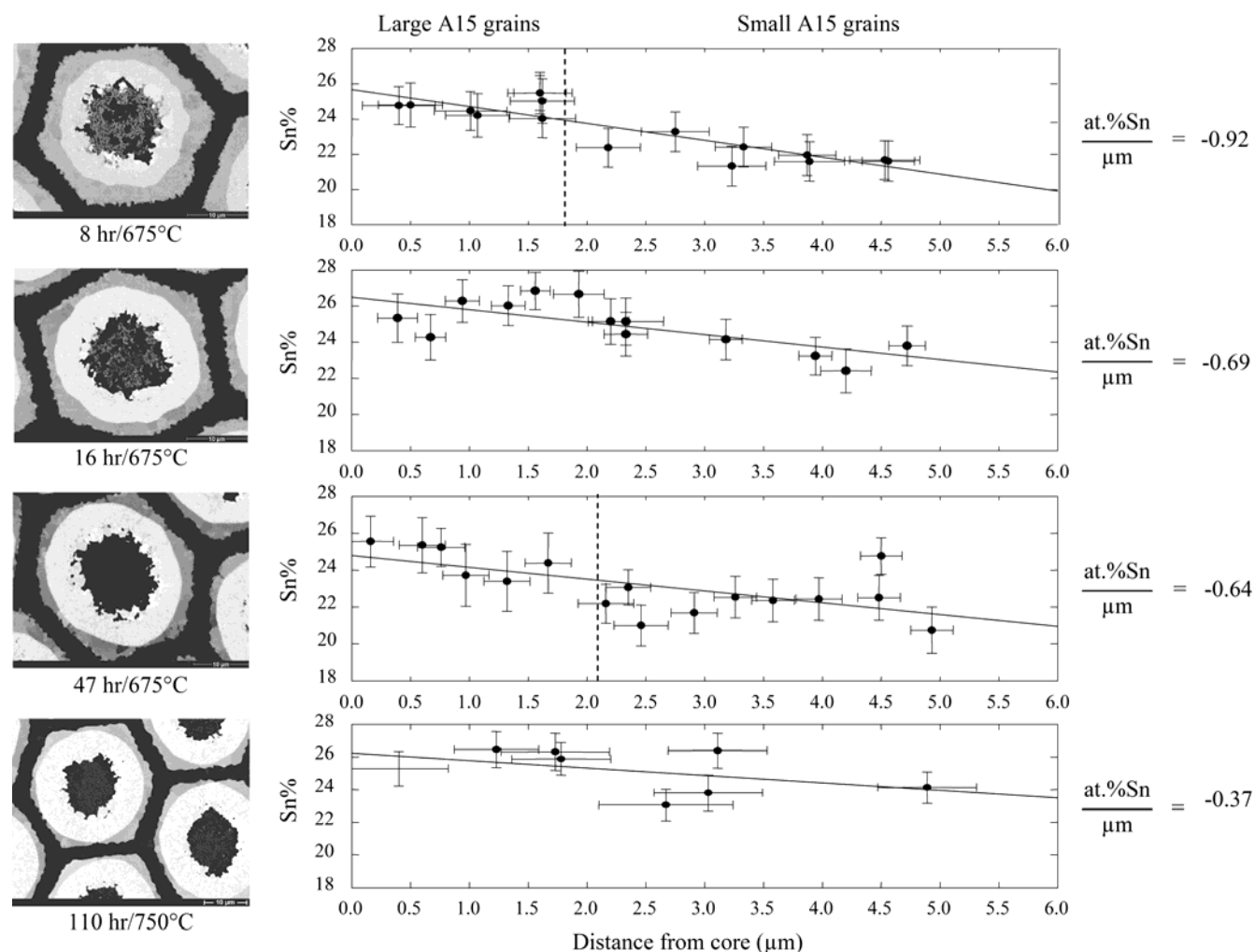


Figure 7. EDX Sn compositions for samples reacted 8 hours at 675°C, 16 hours at 675°C, 47 hours at 675°C, and 110 hours at 750°C. The lines drawn through the points are least squares linear fits to the data. The vertical error bars represent 2σ error in the atomic percent Sn, and the horizontal error bars represent the uncertainty in the distance measurement. Note that these data extend to but do not provide information at the A15-Nb interface.

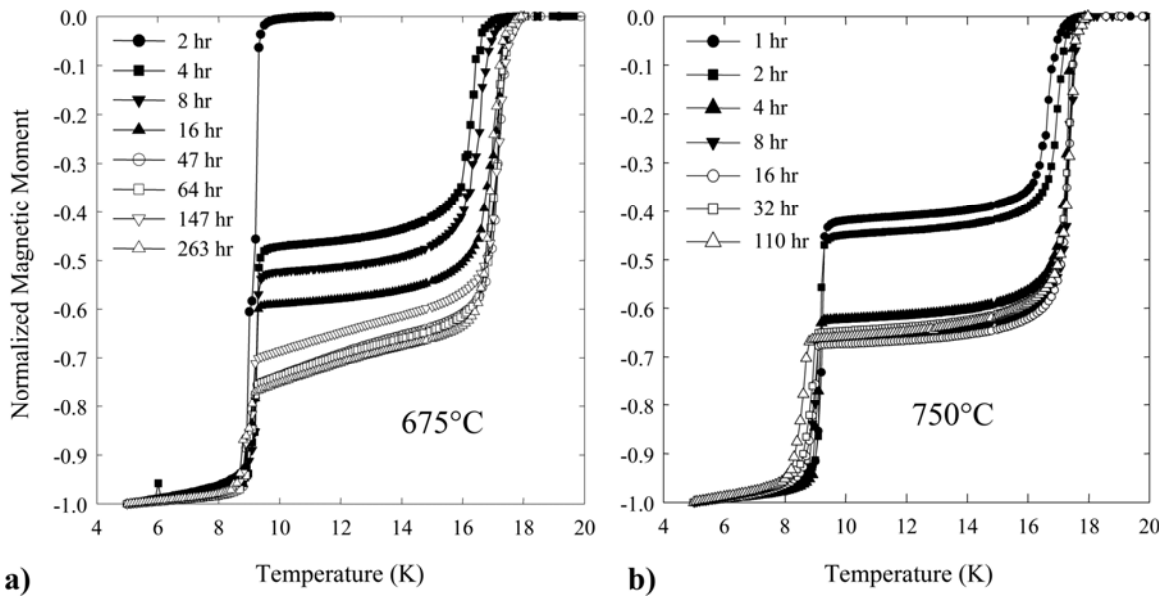


Figure 8. Magnetic moment curves for a) 675°C and b) 750°C heat treatment obtained by zero-field cooling to 5 K and then heating in a field of 1 mT.

this trend associated with the breakdown of circular symmetry in the growing A15 layer when the A15 phase locally breaks though the Nb are seen also in the heat capacity data and will be discussed later.

The $T_c(r)$ plots (figures 10a and 10b for 675°C and 750°C respectively) show that the shorter reactions have a steeper slope and a slightly lower maximum T_c . Starting at 16 hours at 675°C, $T_c(r)$ flattens and there is a general rise of T_c as continued reaction occurs. It is clear however that this occurs after most of the layer growth finishes, since the growth rate declines markedly after 16 hours at 675°C. At 47 hours a distinct tail appears in the T_c trace, corresponding to

the first time at which the A15 phase locally meets the Cu matrix. This tail is a feature of all the longer heat treatments.

The 750°C heat treatment $T_c(r)$ plot (figure 10b) is similar to the 675°C plot. The shorter 1 and 2 hour traces have a steeper slope, $T_c(r)$, and a slightly lower maximum T_c . Starting with the 4 hour plot, $T_c(r)$ flattens and there is a general rise of T_c as continued layer growth occurs. No tail appears for longer heat treatment times, but the broadening and shifting of the “Nb” transition, as it partially converts to Sn-poor A15 phase, is much more pronounced, particularly after 110 hours. An apparent thinning of the A15 layer in the

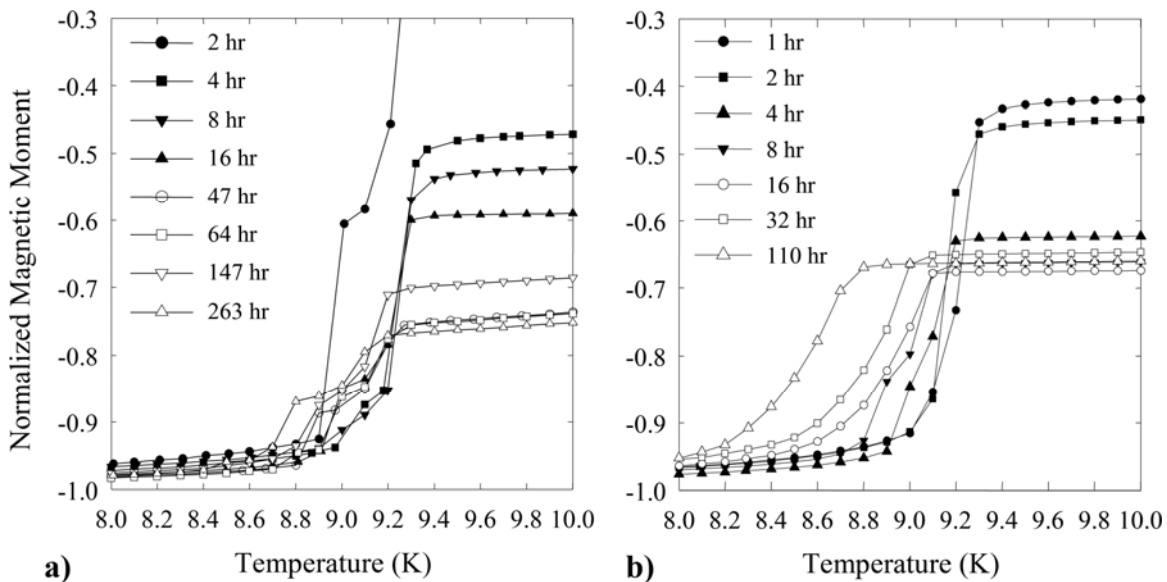


Figure 9. Normalized magnetic moment over the 8-10 K range for heat treatments at a) 675°C, and b) 750°C. The bulk Nb transition is ~9.2 K.

32 and 110 hour heat treatments is also seen, but we believe that this is an artefact of the measurement, as noted later. Overall, the T_c gradient is smaller for the higher temperature reaction.

3.3. Heat Capacity Measurements

The heat capacity curves for 675°C and 750°C heat treatments (figures 11a and 11b respectively) show a steady increase in the magnitude of the jumps at T_c as reaction proceeds. It is also noticeable that the transitions are always sharper for the “Nb” transition than at the onset of the A15 transition. The different magnitudes are due to differences in each sample’s mass. Both figures also show that increasing heat treatment time results in a more pronounced transition at T_c which moves toward higher temperatures. Figure 12 shows that the Nb transition broadens and moves toward lower temperature, in general agreement with the inductive critical temperature data of figure 9. However, the 750°C data shows a continuous reduction in this lower transition with increasing time that is not seen in the 675°C data, thus suggesting a greater conversion of the outer sheath of the filaments to A15 phase with $T_c < 9$ K.

The effect of heat treatment on the high temperature part of the transition is given in figures 13a and 13b. Increasing heat treatment time at 675°C clearly results in a sharper and higher T_c transition, but there is barely any shift for the 750°C heat treatments, which are already sharper than any 675°C sample. It is

clear that this 75°C increase in reaction temperature makes a significant increase in the reaction kinetics.

4. Discussion

An underlying issue in studies of Nb₃Sn is how much more compositionally uniform can the filaments be made and, if they could be made more uniform, how much this would benefit the properties. In terms of maximum critical current there are now have three distinct types of conductors.

Firstly, up to ~ 1 kA/mm² (12 T, 4.2 K), are low hysteresis loss strands with sufficient Cu between filaments to decouple them, these can be bronze process or internal Sn. Using high resolution EDX in TEM samples Abächerli et al. [23] have recently measures very strong compositional gradients in bronze process strands, the Sn composition dropping 7-8 at.% over the < 2 μ m thick A15 annulus. After a 4-5 at.% Sn drop, the Abächerli et al. study indicates that negligible new A15 grain nucleation occurs and a true columnar layer is formed.

Secondly, with up to ~ 2.2 kA/mm² (12 T, 4.2 K), there are the PIT strands that have relatively large (> 30 μ m diameter) filaments. These are the strands in this study. Despite the relatively large filament diameter the Sn supply never drops low enough such that a true columnar layer is formed as in the bronze-process case.

Thirdly, with up to ~ 3 kA/mm² (12 T, 4.2 K), we have the restacked-rod internal Sn strands in which the

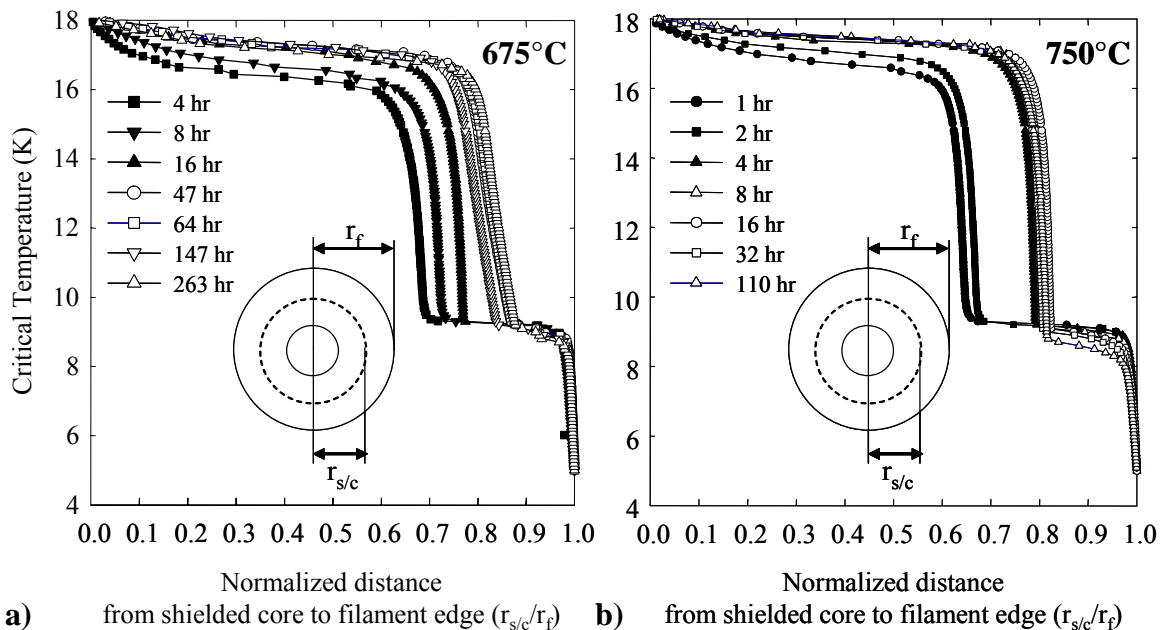


Figure 10. Comparison of the T_c versus radius from DC squid magnetization for the a) 675°C and b) 750°C heat treatments. We assume, (1) circular symmetry, (2) full Meissner shielding by the superconducting layer, and (3) a fully shielded core surrounded by the highest T_c layer.

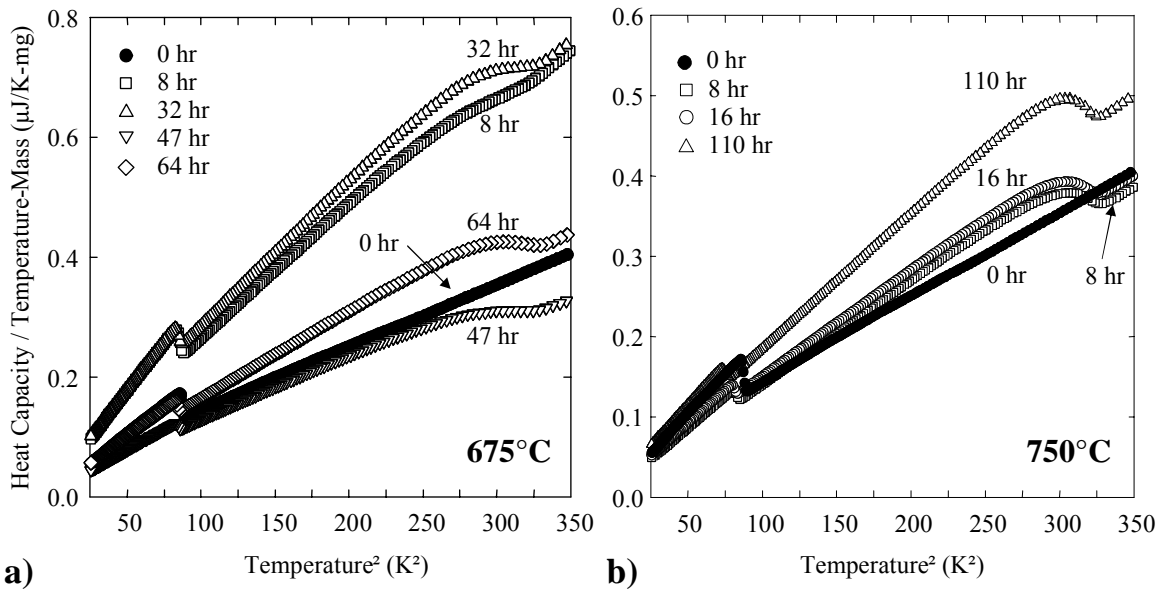


Figure 11. The heat capacity for the a) 675°C and b) 750°C heat treatments. With increasing heat treatment time and temperature the A15 transition ($T^2 \sim 275 - 325 \text{ K}^2$ or $T \sim 16.6 - 18.0 \text{ K}$) becomes sharper and moves to the right.

Cu is so low that the filaments in each sub-element react together to form a single layer of A15. We have recently shown that the overall Sn gradient across the A15 layer in the highest performance rod-restack low-Cu internal Sn design is as low as 0.1 at.% Sn/μm [24], compared with the lowest value reported here of 0.37 at.% Sn/μm. It should be pointed out, however, that the remarkably low overall gradient of 0.1 at.% Sn/μm is somewhat misleading, because in the rod-restack process gradients occur both radially outward from the original Sn core as well as into initial rods that were stacked together to form the sub-element. In fact the onset of the aspect ratio increase

observed $\sim 3.5 \mu\text{m}$ across the A15 layer in figure 6 (that occurred after a Sn drop of $\sim 2.2 \mu\text{m}$) was observed at a distance of $\sim 1.2 \mu\text{m}$ from the original rod centres of a high J_c Rod-in-tube internal Sn strand that had a 12 T (4.2 K) layer J_c of 4000 A/mm^2 [6]. Nevertheless the key geometric difference that allows such low overall Sn gradients in rod-restack design strand is that the Sn has a short-cut between Nb filaments to the outside of the layer (sub-element bundle) and the maximum diffusion distance across the original rods is only the filament radius ($\sim 1-3 \mu\text{m}$).

The importance of using these ECN-PIT type strands for this type of study is their radial symmetry

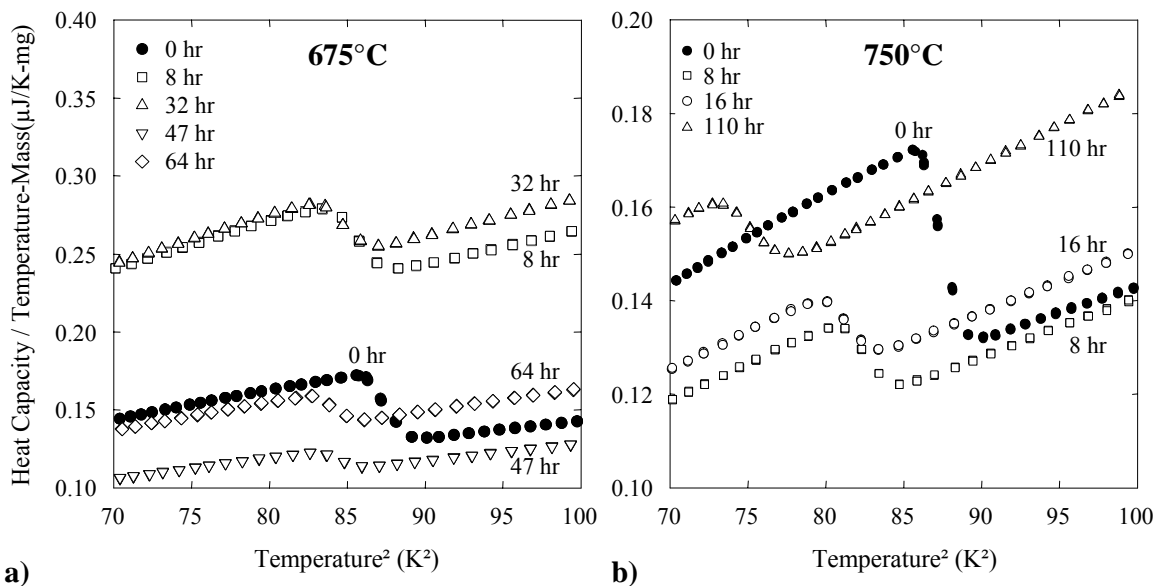


Figure 12. Heat capacity results in the 8.4-10 K (Nb) range for a) 675°C heat treatments, and b) 750°C heat treatments. Bulk Nb transition occurs at $\sim 9.2 \text{ K}$.

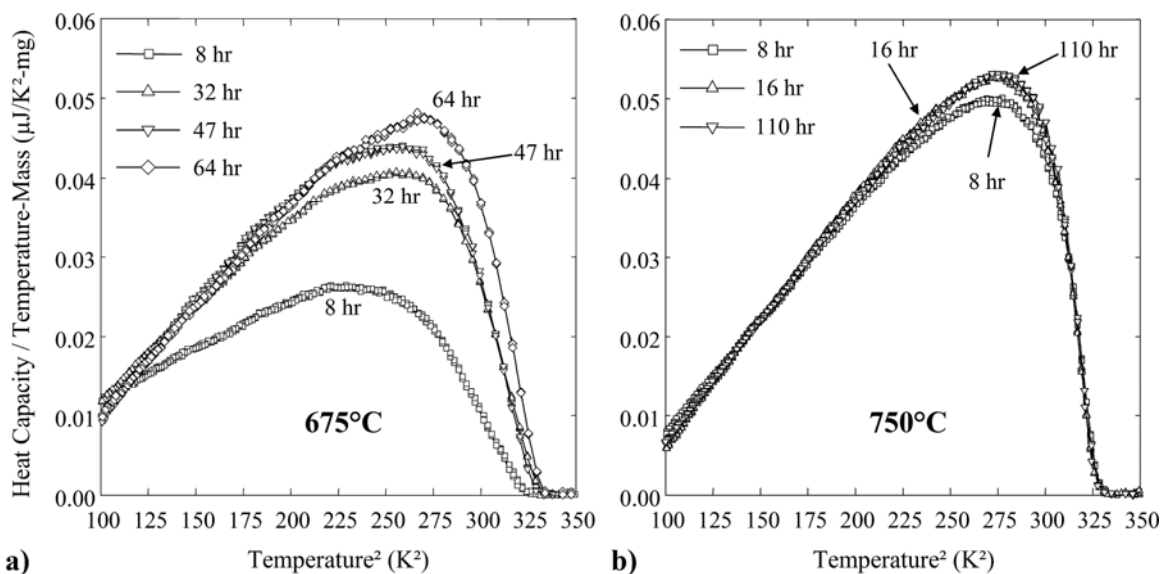


Figure 13. Heat capacity data for the superconducting A15 layer of the a) 675°C and b) 750°C heat treated samples. Heat capacity data due to non-A15 material has been subtracted from the raw data, as noted in text. Transitions become sharper, move towards higher temperatures, and grow in magnitude with increasing heat treatment time. The differences in the magnitude of the curves are due to increases in the amount of A15 phase.

and uniformity allowing us to make the direct property-composition measurements reported here. In fact, the direct correlation of superconducting properties to the local composition of Nb_3Sn filaments is rare [13], [25], [19] and the results are ambiguous. The fact that a high performance PIT conductor has a magnetically transparent design, a Nb_3Sn layer thick enough to quantify using SEM-EDX analysis, and the ability to measure the critical temperature transition using heat capacity makes this design uniquely advantageous. Cooley et al. have additionally been able to exploit the radial homogeneity of this design to successfully model the properties of the strand using a shell model [26].

Nb_6Sn_5 forms very rapidly, appearing after 2 hours at 675°C and being fully consumed after 16 hours. This was also observed by Veringa, et al. [17,27]. This rapid reaction helps grow a 5 μm thick A15 layer in approximately 8 hours, a much thicker and more rapidly grown layer than can be formed by bronze or internal Sn processes. At 750°C the reaction is even faster and the compositional gradient lower but the grain size is too large to achieve high critical current density (grain boundaries are the primary flux-pinning centre in Nb_3Sn).

The Nb-Sn phase diagram [28], suggests that the composition of the A15 should lie over the range 25.5 to 18 at.% Sn, causing a T_c variation from 18 to 6 K across any non-equilibrated layer [11]. The results of figure 7 suggest a linear gradient from 25-25.5 to only 21 at.% Sn over most of the A15 layer, the

composition only diving to lower Sn values very close to the A15-Nb or A15-Cu interface. This small gradient over most of the layer is supported by the results of the inductive critical temperature results of figures 8a and 8b, and the $T_c(r)$ plots in Figs. 10a and 10b. These results show that the bulk of the T_c gradient occurs from 18 to ~14 K range, and that this gradient is flat, consistent with the measured change in composition. These findings are not what might be expected from the results of [11], which would suggest that a Sn composition of 21 at. % corresponds to a T_c of ~9 K. Thus the influence of the measured composition gradient on the superconducting properties appears to be less severe than expected.

The T_c profile does show a greater broadening at the A15-Nb or the A15-Cu interface with increasing heat treatment time. The “Nb transition” also broadens with increasing heat treatment time and temperature, Figs. 9 and 12. Since the solubility of Sn in Nb at 675°C and 750°C is almost nil, according to the phase diagram [28], which would indicate that this is most likely due to the outer Nb layer converting to very Sn-poor A15. Our SEM-EDS measurements show no detectable Sn in the Nb within 0.8 μm of the Nb-A15 interface after 64 hrs at 675°C. However, we do have some visual evidence, from high resolution FESEM BEI images, of Sn diffusion along grain Nb boundaries for internal Sn strand given a final heat treatment of 20 hrs at 700°C [29]. Furthermore, extending the heat treatment time at 675°C to 768 hours for a Nb(Ta) SMI-PIT strand, reduces the Nb transition offset by

~ 0.7 K and broadens the transition width by a factor of 2 while producing a sharp Nb₃Sn transition [30]. Flükiger's T_c measurements on Nb-Sn alloys [31] indicate that a Sn content of as little as 0.2 at.% can reduce the T_c by 0.7 K. Thus the smearing of this transition may result from a combination of Sn-poor A15 and/or localized Sn concentrations in the remaining unreacted Nb tube. Unfortunately, the spatial resolution of the SEM-EDX technique is insufficient to determine the concentration of Sn within 1 μm of the Nb-A15 boundary, and this work suggests that an examination by TEM/STEM would be beneficial.

The fracture images, figure 5, of the 675°C heat treatment show coarse grain A15 near the Sn source (core) and a finer grained A15 moving towards. The EDX data, figure 7, for various times of 675 C heat treatment show a uniform composition gradient over ~ 2 μm , which is approximately the size of the coarse grain region. Earlier work with the PIT method [27],[32] also show that two grain sizes are found, coarse grains near the Sn-rich core and finer grains moving outward from the core. Veringa et al. assert that the large grain A15 is formed in the presence of a liquid Cu-Sn phase, which may be the reason the grains are so large. This is possible given the reaction temperature for the composite. Veringa et al. also state that two different values for the critical temperature were found by Suenaga, one at 17.7 K for the fine grained A15 and one at 18.2 K for the coarse grained A15. However, we find lower T_c when Nb₆Sn₅ is present than when it is absent. The EDX results from the 110 hour / 750°C heat treatment show a gradient which is fairly flat across the layer; the grain size is also much larger, possibly on the order of the layer thickness, probably greater than 2 μm . The large grain size may be the reason why there is no evidence for two composition gradients in the 110 hour / 750°C heat treatment. There seems to be little consequence, in terms of the T_c of the layer, in having two gradients in the layer. However, the two grain sizes will affect J_c . It is clear [9,33] that even the increase of A15 grain size from ~ 150 nm at 675°C to ~ 300 nm at 750°C seriously degrades J_c . Thus it seems highly unlikely that the inner annulus of 1-2 μm A15 grains contributes significantly to J_c .

The deconvolution of T_c employed here is not very satisfactory in spatial terms, because the assumption of full shielding is not valid for thin layers where T_c is rapidly changing. To fulfil the condition of full Meissner shielding in each shell, about 20 penetration depth (λ) thickness layers are needed. In principle, a rigorous calculation could be done, but in fact λ (Sn content) is not known, so such a calculation

would hardly be definitive in yielding the radial variation of T_c . Another defect of using a magnetic deconvolution of T_c is that the radial extent of the superconducting layer in figure 10 is extended due to the shielding of the core. It is clearly seen in the BSE images that the core takes up half the radial distance from the centre of the filament to the outside edge of the filament, while the results of the inductive measurements make it appear that the A15 layer is much thicker. From the 147 hour heat treatment in figure 10a and the 32 and 110 hour heat treatments in figure 10b, it would appear that the A15 layer has thinned compared to the other heat treatments. Backscatter electron images show this not to be the case, and looking at the inductive critical temperature measurements we see that maximum critical temperature has not changed and that the gradient is similar to the rest. Changes in λ near the A15-Nb boundary, thus changing the shielding effects at the interface, may be the cause of this apparent thinning of the A15 layer.

5. Conclusions

1. Inductive critical temperature measurements allowed us to see the growth of the A15 layer inside the filaments of PIT conductor.
2. The $T_c(r)$ plots obtained from the inductive critical temperature measurements are in agreement with the EDX results, showing linear changes in the composition and critical temperature that coincide well with each other.
3. The manufacturer's recommended heat treatment, 47 hr at 675°C, balances the desire to produce a fine A15 grain size (which produces strong flux pinning and thus J_c), with the need to obtain an acceptably high Sn content and small composition gradient giving high T_c and H_{c2} .
4. The microstructure across the fine-grain A15 layer is observed to be uniform until the Sn drops by ~ 2.2 at.% Sn (to ~ 23 at.% Sn), at which point an increased grain aspect ratio is observed.
5. The homogeneity, simplicity and transparency of the PIT design provide an excellent basis for the modelling of this conductor's properties.
6. Significant Sn gradients across the A15 layer appear to be inevitable in this design, which may be mitigated by thinner A15 layers (smaller diameter filaments) and a higher Sn activity from the core.

Acknowledgments

This work was supported through the U.S. Department

of Energy, by both the Department of High Energy Physics under Grant DE-FG02-91ER40643 and the Office of Fusion Energy Sciences under Grant DE-FG02-86ER52131. The authors would like to thank J. H. Lindenhovius of ShapeMetal Innovations (The Netherlands) for fabricating and supplying strand. We also thank Andries den Ouden (University of Twente) for donating additional multifilamentary PIT wire. Alex Gurevich for help in interpreting the inductive critical temperature and heat capacity data and Alex Squitieri for assistance making those measurements. Lance Cooley (now at BNL), Chad Fischer (now at Intel) and Arno Godeke (now at the University of Twente) for additional discussion and Bill Starch for metallographic specimen preparation.

References

- [1] Smathers D B, Marken K R, Larbalestier D C and Evans J 1983, Scanning Auger Investigation of Commercial Multifilamentary Nb₃Sn Conductors," *IEEE Trans. Mag.*, **19(3)** 1421-1424
- [2] Smathers D B 1990, A15 Superconductors, in American Society of Metals: Metals Handbook, Superconductor Materials Science, 10th edition, **2** 1060-1076.
- [3] Parrell J A, Zhang Y, Field M B, Cisek P, Hong 2003, High field Nb₃Sn conductor development at Oxford Superconducting Technology," *IEEE Trans. Appl. Superconductivity*, **13(2)** 3470-3473.
- [4] Parrell J A, Field M B, Zhang Y and Hong S 2004, Nb₃Sn Conductor Development for Fusion and Particle Accelerator Applications, *Adv. Cryo. Eng.*, **50** 369-375.
- [5] Lee P J, Squitieri A A and Larbalestier D C 2000, Nb₃Sn: Macrostructure, Microstructure, and Property Comparisons for Bronze and Internal Sn Process Strands, *IEEE Trans. on Appl. Superconductivity*, **10(1)** 979-982.
- [6] Lee P J, Fischer C M, Naus M T, Jewell M C, Squitieri A A, Larbalestier D C 2003, The Microstructure and Micro-Chemistry of High Critical Current Nb₃Sn Strands Manufactured by the Bronze, Internal-Sn and PIT Techniques, *IEEE Trans. Appl. Superconductivity*, **13(2)** 3422-3425.
- [7] den Ouden A., Wessel S., Krooshoop E., and ten Kate H. 1997, Application of Nb₃Sn superconductors in high-field accelerator magnets, *IEEE Trans. on Appl. Superconductivity*, **7** 733-738
- [8] Barzi E, Limon P J, Yamada R, Zlobin A V, 2001, Study of Nb₃Sn strands for Fermilab's high field dipole models, *IEEE Trans. Appl. Superconductivity*, **11(1)** 3595-3598.
- [9] Godeke A, Jewell M C, Fischer C M, Squitieri A A, Lee P J and Larbalestier D C 2005, The upper critical field of filamentary Nb₃Sn conductors, *J. Appl. Phys.* **97-9**:093909.
- [10] Tachikawa K, Natsuume M, Kuroda Y and Tomori H 1996, Nb₃Sn superconductors prepared from intermediate compound phase, *Cryogenics*, **36(2)** 113-117.
- [11] Devantay H, et al. 1981, The physical and structural properties of superconducting A15-type Nb-Sn alloys, *J. Mat. Sci.*, **16(8)** 2145-2153.
- [12] Flükiger R and Jorda J L 1977, The effects of composition and atomic ordering on superconductivity in the systems Nb₃Ga and V₃G, *Solid State Comm.*, **22** 109-112.
- [13] Hong M, Wu I W, Morris, Jr. L W, Gilbert W, Hassenzahl W V and Taylor C 1982, An Investigation on the Enhancement of the Critical Current Densities in Bronze-Process Nb₃Sn, *Adv. in Cryo. Eng.*, **28** 435-444.
- [14] Wu I W, Dietderich D R, Holthuis J T, Hassenzahl W V and Morris Jr. J W 1983, The Influence of Magnesium Addition to the Bronze on the Critical Current of Bronze-Processed Multifilamentary Nb₃Sn Conductors, *IEEE Trans. Mag.*, **19(3)** 1437-1440,
- [15] Rodrigues Jr. D, Thieme C L H, Pinatti D G and Foner S 1995, Grain boundary compositions, transport and flux pinning of multifilamentary Nb₃Sn wires, *IEEE Trans. Appl. Superconductivity*, **5(2)** 1607-10.
- [16] Lee P J, Hawes C D, Naus M T, Squitieri A A, Larbalestier D C 2001, Compositional and Microstructural Profiles across Nb₃Sn Filaments, *IEEE Trans. on Appl. Superconductivity*, **11(1)** 3671-3674.
- [17] Marken K R, Kwon S-J, Lee P J and Larbalestier D C 1986, Characterization Studies of a Fully Reacted High Bronze-to-Niobium Ratio Filamentary Nb₃Sn Composite, *Adv. in Cryogenic Eng. (Materials)*, **32** 967-975.
- [18] van Wees A C A, Hoogendam P, and Veringa H 1983, Development of high current Nb₃Sn multifilament superconducting material following the ECN powder method, *IEEE Trans. Mag.*, **19** 556-559.
- [19] Cave J R and Weir C A F 1983, Cracking and layer Growth in Nb₃Sn Bronze Route Materials, *IEEE Trans. on Mag.*, **19** 1120-1123.

- [20] Quantum Design PPMS Hardware and Options Manual, Quantum Design (1998).
- [21] Bachmann R, et al. 1972, Heat capacity measurements on small samples at low temperatures, *Rev. Sci. Instruments*, **43** 205-214.
- [22] Lee P J and Larbalestier D C, 2000, Position Normalization As A Tool To Extract Compositional And Microstructural Profiles From Backscatter And Secondary Electron Images, *Microscopy and Microanalysis*, **6**, **Supl. 2** 1026-1027.
- [23] Abächerli V, Uglietti D, Lezza P., Seeber B, Flükiger R, Cantoni M and Buffat P –A 2005, The influence of Ti doping methods on the high field performance of (Nb, Ta Ti)₃Sn multifilamentary wires using Osprey bronze, *IEEE Trans. Applied Superconductivity* **15(2)** 3482-3485.
- [24] Lee P J and Larbalestier 2005, Microstructure, Microchemistry and the Development of Very High Nb₃Sn Layer Critical Current Density, *IEEE Trans. Appl. Superconductivity*, **15(2)** 3474-3477.
- [25] Evetts J E, et al. 1981, Characterization of Nb₃Sn diffusion layer material, *IEEE Trans. Mag.*, **17** 360-363.
- [26] Cooley L D, Fischer C M, Lee P J and Larbalestier D C 2004, Simulations of the effects of tin composition gradients on the superconducting properties of Nb₃Sn conductors, *J. Appl. Phys.*, **96(4)** 2122-2130.
- [27] Veringa H, Hoogendam P, and van-Wees A C A 1983, Growth kinetics and characterization of superconducting properties of multifilament materials made by the ECN powder method, *IEEE Trans. Mag.* **19** 773-776.
- [28] Charlesworth J P, Macphail I, and Madsen P E 1970, Experimental work on the niobium-tin constitution diagram and related studies, *J. Mat. Sci.*, **5** 580-603.
- [29] Lee P J and Larbalestier D C 2005, Microstructural and microchemical homogeneity for high critical current density in Nb₃Sn, in *Progress of Nb-based Superconductors: Proceedings of International Workshop on Nb-Based Superconductors*, Ed. K Inoue, T. Takeuchi and A. Kikuchi, pub. Maeda printing Co. Ltd., Japan, pp. 1-8.
- [30] Veringa H, Hornsveld E M, Hoogendam P 1984, Optimization of high current density A-15 superconductors made by the ECN powder method,” *Adv. in Cryogenic Eng. (Materials)*, **30** 813-821.
- [31] Flükiger R, Phase diagrams of superconducting materials, in Foner S and Schwartz B 1980, *Superconducting Materials Science: Metallurgy, Fabrication, and Applications*, Plenum Press, New York.
- [32] Fischer C M 2002, Investigation of the relationships between superconducting properties and Nb₃Sn reaction conditions in powder-in-tube Nb₃Sn conductors, MSc. Thesis, University of Wisconsin-Madison.
- [33] Fischer C M, Lee P J and Larbalestier D C 2002, Irreversibility field and critical current density as a function of heat treatment time and temperature for a pure niobium powder-in-tube Nb₃Sn conductor, *Adv. Cryogenic Eng.*, **48(B)** 1008-1015.